Impacts of mineral dust on the vertical structure of precipitation

R. Li[1] and Q.-L. Min[1]

Received 16 February 2009; revised 14 December 2009; accepted 24 December 2009; published 11 May 2010.

[1] Characteristics of precipitation vertical structure in deep convective cloud systems are compared using measurements from sensors on board multiple satellites over the equatorial Atlantic under dust-laden and dust-free conditions. Both case and statistical studies consistently show that the impacts of mineral dust on tropical cloud and precipitation systems are highly dependent on rain type. For convective rain, the pattern of rainfall profiles above the dust layer is mainly determined by updraft intensity. For similar updraft intensity, the convective rain at and below the dust layer exhibits enhancement of the breakup process of raindrops due to mineral dust and associated warm air with strong wind shear. For stratiform rain, dust-induced microphysical effects are more evident. For similar storm height (or the rain top), precipitation at altitudes above 6 km is enhanced under dust-laden conditions, suggesting an enhancement of ice heterogeneous nucleation. For warm rain with similar storm height, precipitation is systematically weaker under dust-laden conditions. Furthermore, the ratio of precipitation water to the total amount of atmospheric hydrometeors is smaller under dust-laden conditions. Our study suggests that mineral dust exhibits a second aerosol indirect effect on cloud and precipitation systems.

Citation: Li, R., and Q.-L. Min (2010), Impacts of mineral dust on the vertical structure of precipitation, *J. Geophys. Res.*, *115*, D09203, doi:10.1029/2009JD011925.

1. Introduction

[2] Mineral dust has a significant influence on Earth's radiative balance through direct effects on scattering and absorption of solar and thermal radiation and indirect effects on modulating cloud and precipitation processes [*Denman et al.*, 2007; *Forster et al.*, 2007; *Haywood and Boucher*, 2000]. Studies suggest that a considerable portion of atmospheric mineral dust originates from anthropogenic activities and that mineral dust impacts on clouds have been observed even in the most remote regions of the world [*Denman et al.*, 2007; *Forster et al.*, 2007; *Prospero*, 1999]. Over 65% of global dust emissions come from the Sahara desert in North Africa [*Ginoux et al.*, 2004]. Sahara dust and associated warm and dry air, the Saharan Air Layer (SAL, from near surface to ~5500 m [*Dunion and Velden*, 2004; *D. Liu et al.*, 2008; *Z. Liu et al.*, 2008; *Generoso et al.*, 2008]), interact with cloud systems on its path across the tropical Atlantic Ocean. While measurements in the vicinity of tropical convective systems and hurricanes found that dry air entrainment and vertical wind shear associated with the SAL limited development of tropical storms [*Dunion and Velden*, 2004], very limited in situ data are available to quantify the influence of the SAL on the microphysics of tropical systems, particularly in deep convective systems.

[3] *Rosenfeld et al.* [2001] suggested that mineral dust coated by sulfur may act as additional cloud condensation nuclei (CCN), decreasing the size of the cloud droplet and consequently suppressing and delaying the warm rain process because of the reduction of cloud drop coalescence efficiency. Such indirect effects of aerosols are also observed in smoke [*Rosenfeld*, 1999; *Yin et al.*, 2000; *Andreae et al.*, 2004; *Teller and Levin*, 2006] and air pollution cases [*Rosenfeld*, 2000]. Dust particles also can act as giant CCNs (GCCN) to enhance precipitation by producing large cloud drops. In the modeling study of *Teller and Levin* [2006], the GCCN effect is partially canceled out by the CCN effect. Additionally, mineral dust can act as effective ice nuclei (IN) to enhance the heterogeneous nucleation process, producing more ice particles at warmer temperatures and at lower supersaturation conditions [*DeMott et al.*, 2003; *Sassen et al.*, 2003; *Sassen*, 2005]. Using a cloud resolving model, *van den Heever et al.* [2006] found that the IN effect plays an important role in determining the inner structure of the cloud system and the combined effects of CCN, GCCN, and IN on the cloud system strongly depend on the cloud evolution stage. At early stages, the rain intensity (rain mixing ratio) was generally weaker under aerosol conditions than that under clean conditions. However, at later stages, the rain intensity under aerosol conditions was greater. Recently, *Rosenfeld et al.* [2008] hypothesized that suppression of rain by aerosol at an early stage may consequently invigorate convective clouds and produce more rainfall at later stages.

[4] Microphysical processes associated with dust-cloud interactions affect cloud hydrometeor profiles and water

[1]Atmospheric Sciences Research Center, State University of New York at Albany, Albany, New York, USA.

0148-0227/10/2009JD011925

phase changes, which in turn alter the cloud dynamics and thermodynamics through latent heat release [*van den Heever et al.*, 2006; *Rosenfeld et al.*, 2008]. Potential vorticity in the tropics is directly proportional to the local vertical gradient in the heating profile [*Haynes and McIntyre*, 1987; *Mapes and Houze*, 1995]. Such vorticity further influences the large-scale dynamics [*Wu and Sarachik*, 2000]. The vertical precipitation profiles reflect the combined effects of dynamic, thermodynamic, and microphysical processes in cloud systems [*Fu and Liu*, 2001; *Liu and Fu*, 2001]. Furthermore, as the various aerosol indirect effects on clouds and precipitation exhibit distinct vertical characteristics (i.e., the CCN and GCCN effects dominate at lower layers and the IN effect is at upper layers), it is crucial to assess and understand those effects on vertical structures of cloud systems.

[5] A difficulty in substantiating dust effects on clouds and precipitation is that cloud evolution can be affected profoundly not only by mineral dust but also by cloud dynamics and thermodynamics. Current precipitation measurements from space come primarily from low-orbit satellites, which cannot provide continuous observation of the entire evolution of storm systems. However, precipitation profiles measured from precipitation radar (PR) on the Tropical Rainfall Measuring Mission (TRMM) satellite can be separated into convective and stratiform rain regimes. The young, active, and violent convection-related rain is identified as convective rain. The older, inactive, and weak convection-related rain is identified as stratiform rain. The updraft velocity associated with convective rain is strong (1–10 m/s), while updraft in stratiform rain is weak (<1 m/s) [*Houze*, 1997]. Separation of rain regimes provides a measure of the evolutionary stage of convection and a unique opportunity to study the aerosol indirect effect on precipitation at different evolutionary stages.

[6] Recently, *Min et al.* [2009] utilized multisensor observations to investigate the impact of mineral dust on precipitation internal structures and microphysical interaction in a case study. They hypothesized that dust particles transferred to a high altitude by strong convection act as effective ice nuclei, enhance heterogeneous nucleation, and consequently, produce more stratiform rain particles than that in the absence of dust.

[7] While the case study by *Min et al.* [2009] shines light on detailed physical processes, a statistical investigation will confirm the validity at large time scale and will exclude chance correlation. In this paper, we extend the study of *Min et al.* [2009] to more cases by employing observations from both the TRMM and Aqua satellites. Specifically, we utilize passive microwave measurements of precipitation vertical structure from both the TRMM Microwave Imager (TMI) and the Aqua Advanced Microwave Scanning Radiometer for EOS (AMSR-E) to conduct a statistical study, as passive microwave sensors have larger spatial and higher-frequency coverage than the active precipitation radar. Furthermore, we focus on liquid phase precipitation processes, where retrievals of passive microwave measurements from both TRMM TMI and Aqua AMSR-E are well validated.

2. Methodology and Measurements

2.1. Dust Event and Research Domain

[8] A transatlantic Saharan dust outbreak occurred on 1–7 March 2004. The mineral dust interacted with cloud systems as the dust layer traveled across the tropical eastern Atlantic Ocean. Thermodynamic, dynamic, and cloud microphysics observations of the dust layer and cloud systems were gathered by several satellites, including the TRMM, Terra and Aqua, and Meteosat-8, and by a few Aerosol Robotic Network (AERONET) stations.

[9] A set of red-green-blue (RGB) composite images from the Spanning Enhanced Visible and Infrared Imager (SEVIRI) on the Meteosat-8 satellite shows the outbreak, development, and transportation of Saharan dust and its interaction with cloud systems at 15 min intervals. Based on the sequence of the RGB images from Meteosat-8 around TRMM and Aqua overpass times, three tropical deep convection cases (one from TRMM, two from Aqua) during the dust event were found for the case study. For the case observed by TRMM, as illustrated in Figure 1a, a Meteosat-8 RGB composite image at 0912 UTC shows a deep convection system (blue and white) with convective and stratiform rain segments interacting with a dust plume in the northern sector and more pristine marine air in the southern sector. The intersection occurred as the system moved northwest and the dust storm spread southward toward the equator.

[10] To investigate the vertical structure of precipitation in the deep convective system, multisensor measurements from the TRMM satellite were used to provide cloud and precipitation profile information [*Kummerow et al.*, 1998, 2000]. Figure 1b shows a surface rain rate image of TMI at about 0911 UTC, in which two parallel lines indicate the swath of PR. The PR, a Ku band precipitation radar with a swath of about 215 km, provides hydrometeor reflectivity profiles with a vertical resolution of 250 m and a horizontal footprint of 4.3 km at its nadir.

[11] The Moderate Resolution Imaging Spectroradiometers (MODIS) on board both Terra and Aqua satellites provide assessments of aerosol and cloud properties during the dust event. As shown in Figure 1c, the zonal averaged column aerosol optical depth (AOD) in the vicinity of the cloud system, deduced from Terra at about 0955 UTC on 8 March 2004, decreased substantially from 4°N to 1°S and was almost constant farther south. It is extremely difficult to determine aerosol concentration in the subcloud layer directly from satellite observation. We assumed that the dust concentration in the cloud area is similar to that in the nearby cloud-free area. For the TRMM observed case, we selected the region of 4°S–4°N and 10°W–5°E (magenta box in Figure 1a) as the research domain for the case study, where the section from 4°N to 0.5°S was influenced by the dust plume as the dust sector (DS) and the section from 1°S and 4°S was in the relatively pristine marine air as the dust-free sector (DF). Although there were some hot spots along the dust storm track, the Terra MODIS retrievals indicate that the 550 nm coarse mode AODs were much larger than the fine-mode AODs. Therefore, the dominant aerosols were mineral dust rather than smoke aerosols. Ship-based measurements of the SAL in this dust event are given by *Nalli et al.* [2005, 2006] and *Morris et al.* [2006]. The characteristics of cloud and precipitation in a fixed domain from 4°N to 1°S and from 10°W to 5°E are also analyzed using both TMI and AMSR-E data for the entire dust event. On the basis of the domain-averaged aerosol optical depth, shown in Figure 1d, the time series of the event are further segregated into a

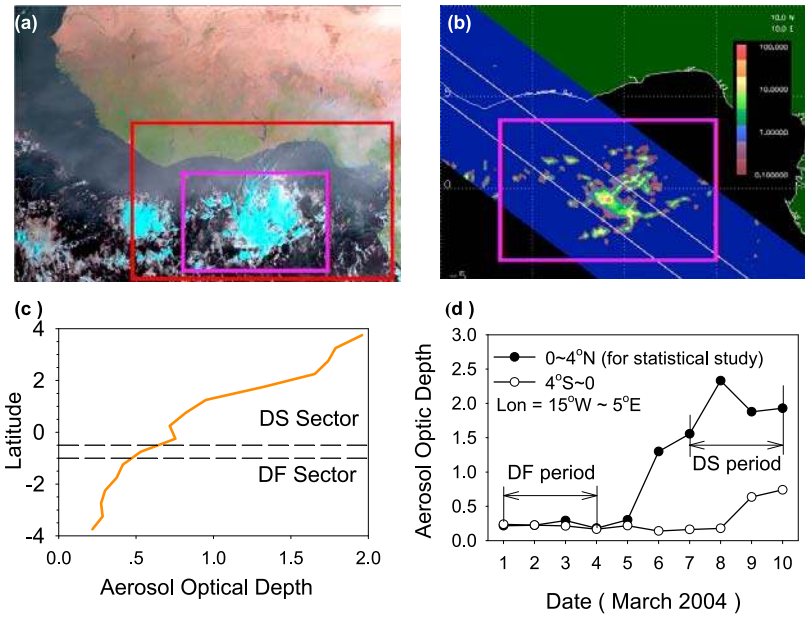

Figure 1. (a) Meteosat-8 red-green-blue (RGB) composite visible image at 0912 UTC on 8 March 2004. (b) TRMM Microwave Imager (TMI) precipitation image on orbital 35979 at 0911 UTC data (TRMM PR swath indicated by the two gray lines). (c) Zonal-averaged column aerosol optical depth retrieved from Moderate Resolution Imaging Spectroradiometer on EOS (MODIS) at 0955 UTC in the study domain (i.e., magenta box in Figure 1b). Dashed lines indicate the dividing lines between the selected dust (DS) sector and dust-free (DF) sector. (d) Time series of area-averaged column aerosol optical depth retrieved from MODIS during 1–10 March 2004.

dust-free period (1–4 March) and a dust period (7–10 March) for the statistical study.

2.2. Active and Passive Microwave Retrievals of Rainfall Vertical Structure

[12] In this study, we used standard products from TRMM PR, 2A25, which provide 3-D structures of rain rate. *Min et al.* [2009] directly used the PR attenuation-corrected reflectivity (Ze) to investigate the evolution of precipitation-sized hydrometeors under both dust-laden and dust-free conditions. This reflectivity represents the combined effect of hydrometeor effective size and total amount. Using a prescribed reflectivity-rain rate (Ze-R) relationship, the rain rate is retrieved from PR reflectivity [*Iguchi et al.*, 2000]. Since the initial choice of the Ze-R relationship for each rain type affects the rain estimates substantially [*Ulbrich and Atlas*, 2007, 2008], dust-induced microphysical changes may alter the Ze-R relationship. Although the accuracy of rain rate estimates from the PR may be limited by dust contamination, the systematical differences between dust-laden and dust-free sectors are our focus and provide useful analysis on mineral dust impacts. Using the rain rate instead of the attenuation-corrected reflectivity also provides more quantitative assessment of mineral dust impacts.

[13] An advantage of the PR rainfall product is the separation of convective and stratiform rain. The stratiform rain is associated with the features of radar bright band and weak radar reflectivity, which indicate weak vertical mixing and weak updraft velocity. The convective rain is associated with strong radar reflectivity, which is related to more and/or large particles requiring strong updraft velocity to lift them [*Awaka et al.*, 1997]. Additionally, differences of the horizontal pattern of convective and stratiform rain are also employed to separate them from each other [*Steiner et al.*, 1995]. The PR rainfall product also contains a third rain type called "other type." Since "other type" contributes little to the total rainfall, we do not include it into our statistics. To further constrain rain types, we define the rain top or storm height (SH) as the beginning height of three continuous bins with detectable rain echo and classify the rainfall with SH below 4 km (close to the freezing level in this study) as "warm rain" regimes. The warm rain does not involve the rain-forming process of ice phase; thus, it is used to understand the CCN effects of mineral dusts on precipitation.

[14] Rainfall vertical structures are also estimated from TMI, which has five wavelength channels of 10.7, 19.3, 21.3, 37.0, and 85.5 GHz with a wider swath of about 780 km [*Kummerow et al.*, 1998]. The TMI 2A12 product is utilized in the study in which the surface rain rate (with convective rain contribution) and vertical profiles of cloud liquid water, precipitation water, cloud ice water, and precipitation ice at 14 layers are retrieved using the Goddard profiling algorithm (GPROF) [*Kummerow et al.*, 2001]. The vertical resolutions of TMI profiles are 0.5 km below 4 km, 1.0 km between 4 and 6 km, 2.0 km above 6 km, and 4.0 km above 10 km, respectively. Relatively small uncertainty exists in TMI-retrieved liquid phase hydrometer profiles, as indicated by validation against the PR profiles [*Kummerow et al.*, 2001]. Therefore, only the liquid phase portion of the hydrometer (i.e., the precipitation water) profiles is investigated. To increase measurement samples, cloud and

Table 1. Sample Statistics and Mean Surface Intensity for the Case Studies[a]

		Convective Rains		Stratiform Rains		Warm Rains	
	Sector	Sample	Intensity[b]	Sample	Intensity[b]	Sample	Intensity[b]
PR	DS	247 (0.8%)	7.98	753 (5.6%)	1.91	67	0.69
	DF	159 (0%)	15.26	626 (3.5%)	2.71	78	1.33
TMI	DS	416	0.27	1230	0.057		
	DF	165	0.36	396	0.086		
AMSR-E I	DS	129	0.19	206	0.026		
	DF	289	0.26	503	0.040		
AMSR-E II	DS	102	0.25	191	0.035		
	DF	171	0.37	132	0.053		

[a]Values in parentheses are percentages of those profiles having no detectable rains at 1.5 km altitude).
[b]The surface rain intensity stands for mean rain rate (mm/h) for PR, but mean precipitation water (g/m^3) for TMI and AMSRE.

rainfall vertical structures derived from AMSR-E (those retrievals are provided by C. D. Kummerow (personal communication, 2006)) on board Aqua with the GPROF algorithms are also analyzed. The same analysis procedure for TMI is applied to the AMSR-E products. Both TMI and AMSR-E rainfall data are further classified into convective rain and stratiform rains. Samples with the estimated convective rain fraction larger than 70% are classified as convective rains. The threshold of 70% is quite arbitrary, and a sensitivity test with different thresholds from 60% to 80% indicates that it will not affect our final conclusion.

2.3. Constraints on Dynamic and Thermodynamic Conditions

[15] Since microphysical and dynamical factors are often intermingled, distinguishing the two requires either special circumstances (e.g., a uniform cloud field that is only perturbed in certain locations by dust) or statistical analysis of a sufficiently large amount of data in a specific cloud dynamic regime. In this study, we attempted to separate the possible dynamic and thermodynamic impacts from the aerosol effects in three ways.

[16] First, from numerous satellite observations we selected three mesoscale convective systems (MCS) that were partially polluted by the Saharan dust plume and focused on the difference of precipitation features between the dust-laden (DS) and dust-free (DF) portions. The dynamic variations within the same system in different portions should be generally smaller than those among different storm systems in different times and locations.

[17] Second, each convective cell in MCS goes through a life cycle including formative stage, intensifying stage, mature stage, and decaying stage. The separation of stratiform and convective rain itself provides the constraints on cloud evolution. Hence, we separated convective and stratiform clouds and studied the relationship between these two rain regimes under the influence of mineral dust.

[18] Currently, there is no direct measure of convective strength from satellite measurements. However, several well-tested proxy parameters directly inferred from active and passive microwave measurements provide information of updraft intensities for each convective cell, such as the maximum height of 30 dBZ (Hmax30) and the polarization corrected brightness temperature at 85.5 GHz (PCT85) [*Nesbitt and Cecil*, 2000; *Cecil et al.*, 2005; *Zipser et al.*, 2006]. A higher Hmax30 indicates large and/or more particles can be lifted to a higher altitude because of strong convection, while a lower PCT85 indicates more ice aloft in the upper layer of convective cells. Thus, we used both parameters as indicators of convective strength. However, the updrafts in most stratiform rain are weak, resulting in the maximum reflectivity less than 30 dBZ. For stratiform rain, we used the SH as an indicator, i.e., the higher SH the stronger the updraft. Also, we used the near-surface rain rate (at 1.5 km altitude for PR observations) and near-surface

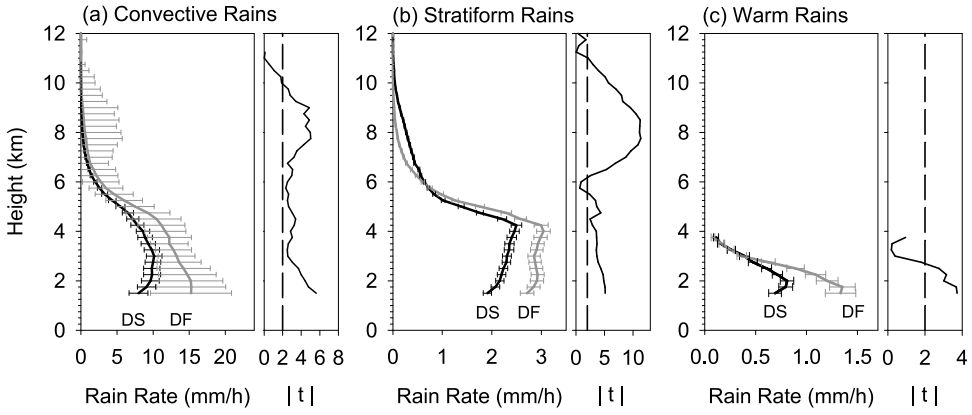

Figure 2. Mean profiles and standard error in DS and DF sectors as seen by TRMM PR for (a) convective rains, (b) stratiform rain, and (c) warm rains. The *t* testing significances of difference are also shown (dashed line indicates the 95% confidence level at 60 degrees of freedom).

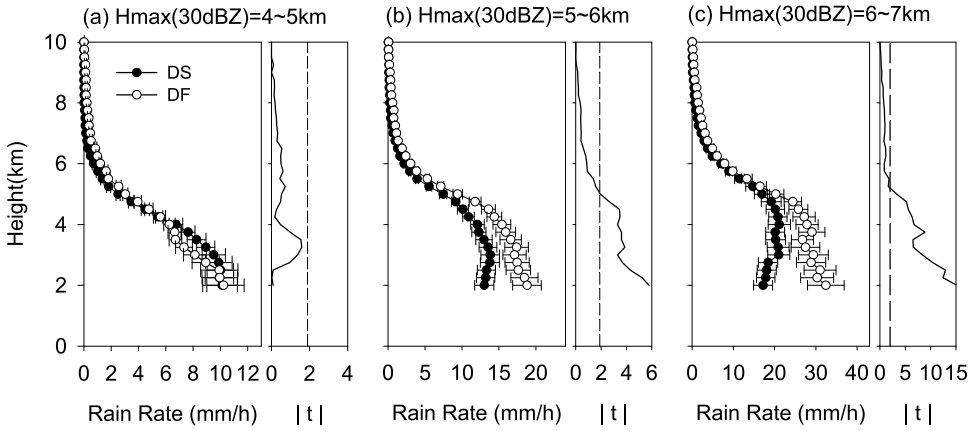

Figure 3. Convective rain profiles as seen by TRMM PR with given maximum height of 30 dBZ ranging at (a) 4–5 km, (b) 5–6 km, and (c) 6–7 km. The *t* testing significances of difference are also shown (dashed line indicates the 95% confidence level at 60 degrees of freedom).

rain mixing ratio (at 0.5 km altitude for TMI observations) as additional constraints of dynamic strength.

3. Results

3.1. Rain Rate Profiles From TRMM PR

[19] The case observed by TRMM on 8 March 2008 has been analyzed extensively by *Min et al.* [2009] using the TRMM PR attenuation-corrected reflectivity. Here we directly use rain rates retrieved from PR to assess the impacts of mineral dust on precipitation directly and to establish the linkage between passive microwave retrievals with the active PR retrievals. Since the TRMM PR cannot detect surface rain because of the surface return contamination, only rain rate measurements above 1.5 km altitude (free from surface clutter) are used. The samples of convective

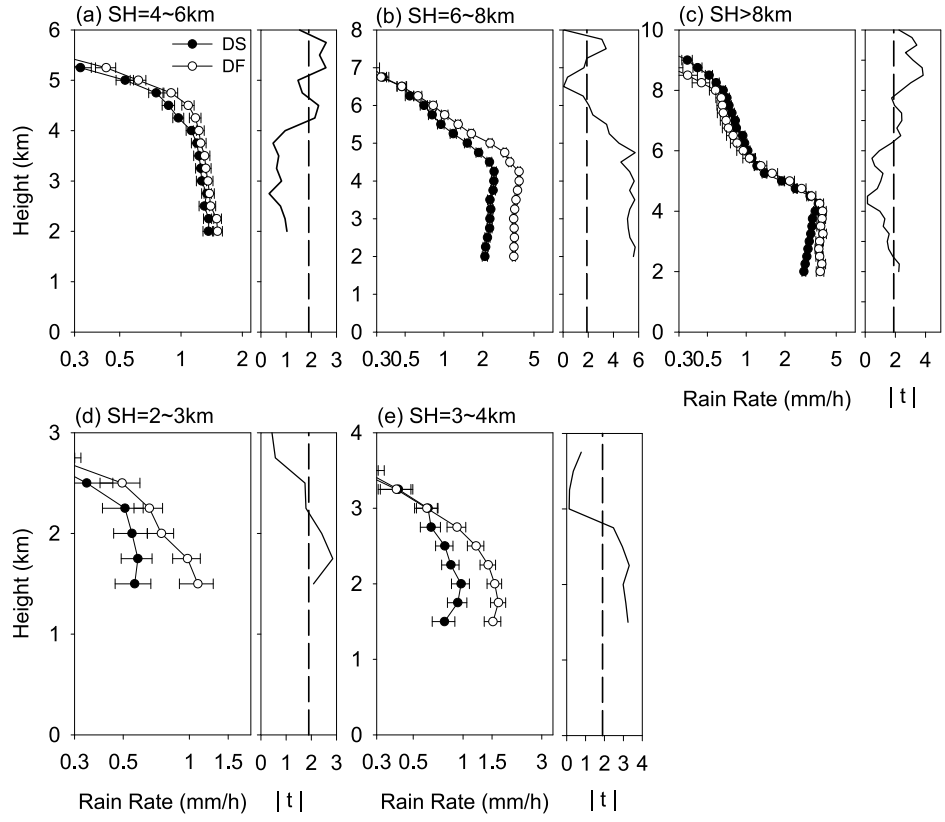

Figure 4. (top) Stratiform rain profiles and (bottom) warm rain profiles as seen by TRMM PR with given storm height ranging from (a) 4–6 km, (b) 6–8 km, (c) above 8 km, (d) 2–3 km, and (e) 3–4 km. The *t* testing significances of difference are also shown (dashed line indicates the 95% confidence level at 60 degrees of freedom).

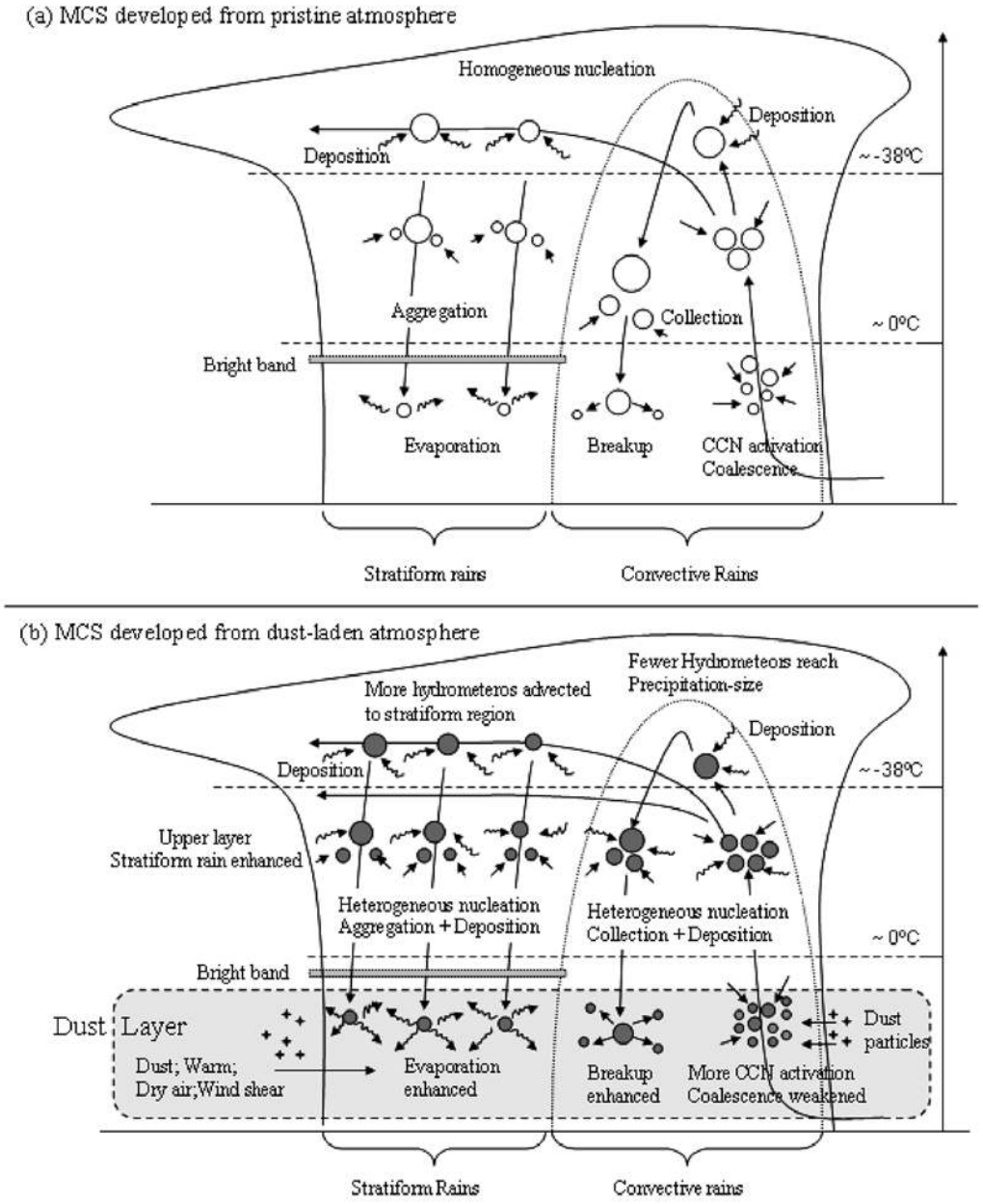

Figure 5. Schematics to show the proposed impacts of mineral dust on the vertical structure of precipitation in mesoscale convective system (MCS): (a) MCS developed from pristine atmosphere and (b) MCS developed from dust-laden atmosphere.

and stratiform rain in the DS sector are comparable with those in the DF sector, listed in Table 1, while warm rain samples in the DS sector are fewer than that in the DF sector. However, the partition of warm rain sample to the total rain sample in the DS sector is 0.06 and 33.3% less than 0.09 in the DF sector, suggesting possible suppression of shallow convective rain process due to mineral dust [*Rosenfeld et al.*, 2001].

[20] Figure 2 shows the overall mean rain rate profiles for three different rain regimes in both the DS and DF sectors. The rain rates in both convective and stratiform rain show two distinct gradients with decreasing height toward the surface: a mild increase above 6 km and a steep increase between 4 and 6 km, reflecting two possible raindrop growth mechanisms of water vapor deposition and aggregation of ice [*Fu and Liu*, 2001; *Liu and Fu*, 2001]. Below the freezing level at about 4 km the rain rate in the convective rain keeps increasing toward a certain height (~3 km for rain in DS and ~2 km in DF), while the rain rate in the stratiform rain reaches a maximum around the freezing level and then decreases.

[21] Substantial differences of rainfall profiles between the DS and DF sectors are clearly evident. For convective rain, the mean rain rate in the DS sector is weaker than that in the DF sector at all altitudes. In contrast, the mean intensity for the stratiform rain in the DS sector is significantly stronger in the upper portion (above 6 km, with 536 and 434 samples in DS and DF sectors, respectively) but

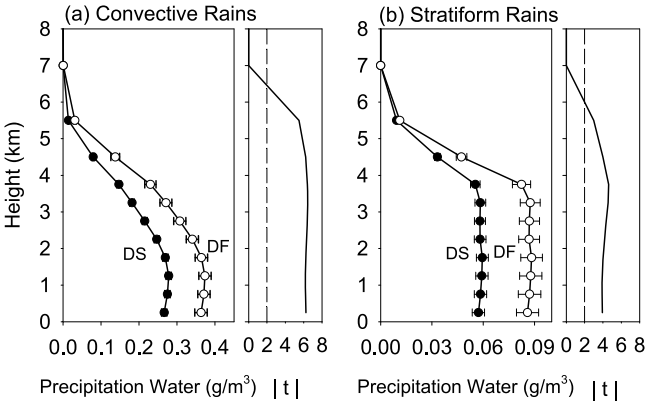

Figure 6. TMI-retrieved precipitation water profiles and standard error of (a) convective rain and (b) stratiform rain in DS and DF sectors. The *t* testing significances of difference are also shown (dashed line indicates the 95% confidence level at 60 degrees of freedom).

weaker in the lower portion (below 5 km). Most of the rain rates above 6 km are in ice phase [*Petersen and Rutledge*, 2001], illustrating that there are more and/or larger ice precipitation-sized particles aloft in the upper portion of stratiform rain in the DS sector than in the DF sector. This phenomenon is generally consistent with model simulations by *van den Heever et al.* [2006] (i.e., the enhancement of rain rate above ~4.5 km in their Figures 11b and 11d), although the stratiform rain was not separated from convective rain in their simulations. Also, the convective rain rate near the lowest altitudes appears to be decreasing in the DS sector but not in the DF sector. For warm rains, the mean rain rate in the DS sector is substantially weaker than that in the DF sector.

[22] These observed differences can be attributed to thermodynamic and dynamic effects related to the particular SAL features [*Dunion and Velden*, 2004] and/or to microphysical effects related to the distinct dust loading. The enhancement of precipitation at high altitudes can be the consequence of aerosol IN effects of enhancing ice phase hydrometeors from model sensitivity studies [*van den Heever et al.*, 2006]. However, without detailed in situ measurements of dynamic condition and model simulations, it is impossible to completely untangle those two effects. Here, we attempt to understand observed changes under the constraints of updraft intensity proxies.

[23] Profiles of convective rain with elevated Hmax30 (proxy of updraft intensity) are shown in Figure 3. Comparing with the large variation of rainfall profiles shown in Figure 2a, it is clear that by applying the constraint of Hmax30, the variability of rain rate at each altitude (i.e., the error bar) decreases substantially. It indicates that Hmax30 is a good indicator of updraft intensity. Particularly, the profiles at upper layers above ~5 km show similar patterns in the DS and DF sectors, indicating that the convective rain profiles generally are determined by updraft intensity. However, at lower layers, from mild convection (Hmax = 5–6 km) to strong convection (Hmax = 6–7 km), the differences of rainfall profiles between the DS and DF sectors increase markedly. The differences are clear at low altitudes below 5 km from the downward increasing in the DF sector to the downward decreasing in the DS sector, particularly for strong convection. The decrease in rain rate downward in the DS sector starts at about 3 km, where the SAL is located, suggesting a possible enhancement of raindrop breakup and/or evaporation processes due to the presence of mineral dust and associated strong wind shear and of dry and warm air [*Dunion and Velden*, 2004].

[24] Similarly, the stratiform rainfall profiles in the DS sector are different from those in the DF sector, shown in Figures 4a–4c, under the same constraint of storm height. It

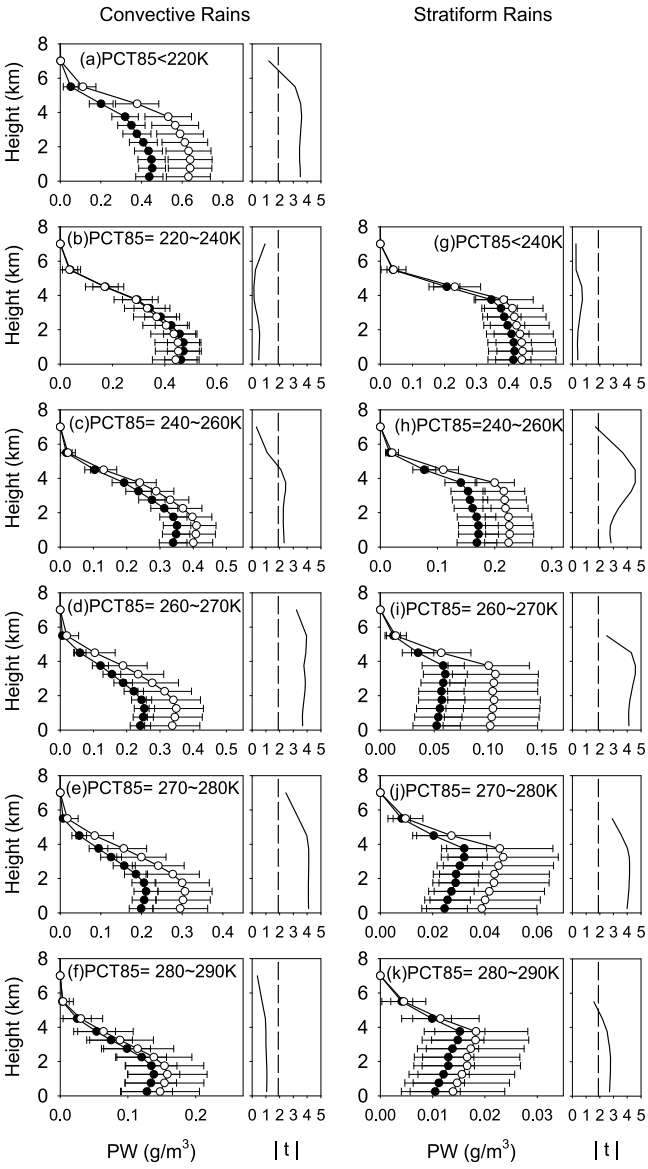

Figure 7. TMI retrieved precipitation water profiles of convective rain with given polarization-corrected brightness temperature at 85.5 GHz (PCT85) in the ranges of (a) <220 K, (b) 220–240 K, (c) 240–260 K, (d) 260–270 K, (e) 270–280 K, (f) 280–290 K and of stratiform rain with given PCT85 in the ranges of (g) < 240 k, (h) 240–260 k, (i) 260–270 k, (j) 270–280 k, and (k) 280–290 k. The *t* testing significances of difference are also shown (dashed line indicates the 95% confidence level at 60 degrees of freedom).

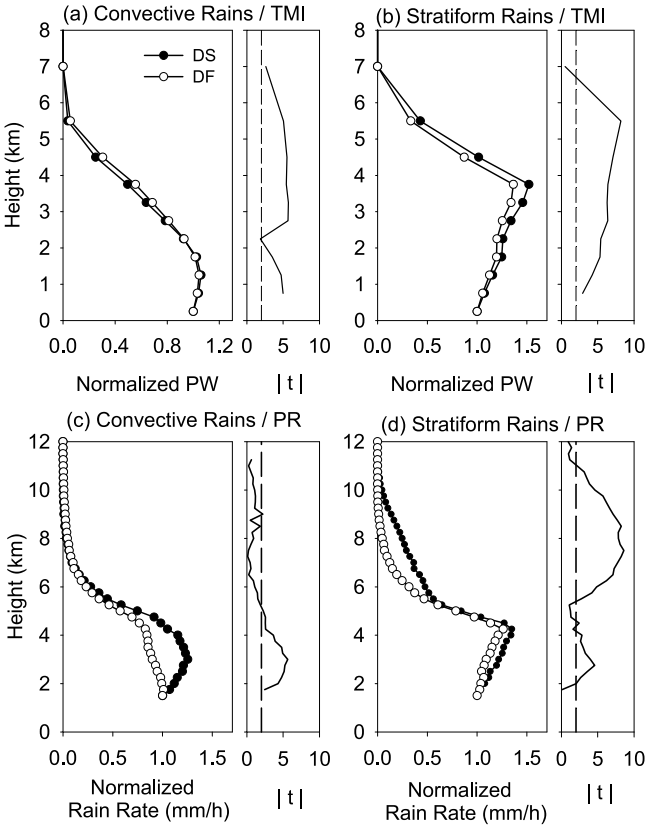

Figure 8. Normalized mean TMI precipitation water profiles and normalized mean PR rain rate profiles (with standard error) of (a, c) convective rain and (b, d) stratiform rain in DS and DF sectors. The *t* testing significances of difference are also shown (dashed line indicates the 95% confidence level at 60 degrees of freedom).

illustrates that the rainfall growth processes are different under dust conditions. Particularly, for rain that is formed at high altitudes (SH > 8 km), the rain rates under the influence of mineral dust are significantly greater than the pristine counterpart. For similar dynamical conditions, the enhancement of rain rate under dust conditions occurs at altitudes where ice nucleation processes dominate (Figure 4c). It implies a potential role of mineral dust in the microphysical processes of rain formation. For warm rain, the suppression of warm rain under dust conditions is evident. This could be due to the microphysical processes of dust CCN effect or the thermodynamic effect of dry and warm SAL or both, which warrant further investigation.

[25] Figure 5 shows schematics of microphysical processes of precipitation formation for both pristine and dust-laden scenarios. Dust particles, particularly those coated by sulfate after traveling through polluted air, are effective cloud condensation nuclei. Aerosols increase the number concentration of cloud droplets and decrease their sizes [*Twomey*, 1977], reducing the coalescence efficiency of raindrops [*Rosenfeld et al.*, 2001]. This mechanism occurs in the warm rain process shown in Figures 4d and 4e. The same mechanism may also occur in deep convective rain. However, it is not apparent in Figure 3a because the dynamic-induced variation in convective rain is so strong that such an impact becomes ambiguous. When more mineral dust is lifted by convection to higher altitudes, those particles act as effective IN to form more ice particles through a heterogeneous nucleation process [*DeMott et al.*, 2003; *Sassen et al.*, 2003]. However, those nucleated particles in convective cores may experience less growth through vapor deposition in the dusty environment due to the vapor competition among the dust-enhanced nuclei concentration. Those hydrometeors in convective rain grow in limited sizes and cannot be detectable by the PR because their reflectivity was below the PR detection threshold (~17 dBZ). For a given updraft intensity, no detectable difference of convective rain rate above ~5 km can be found between the DS and DF sectors (Figures 3b and 3c). When nucleated small ice particles advected into the stratiform region with the convection outflows, sufficient time had elapsed to allow the growth of ice crystals to sizes detectable by the PR. This is evident by the high rain rate observed in the stratiform dust region (Figures 2b and 4c). On the contrary, in the dust-free sector, nuclei concentration is lower, and the growth to PR detectable sizes is more rapid in the convective region, resulting in a strong rain rate.

[26] Additionally, the stratiform rain rate in low layers decreases toward the surface with a much steeper rate (Figures 4c) in the DS sector. The warm rain regime also illustrates similar behavior (Figures 4e). The raindrop evaporation and/or breakup processes can reduce the rain rate toward the surface. Both mechanisms can be substantially enhanced by the mineral dust and associated dry and warm air with strong wind shear. However, the single-wavelength radar system of the PR limits its capability to distinguish particle sizes of precipitation. We will further investigate raindrop evaporation and breakup processes at low altitudes by combining PR measured rain rate with the TMI retrievals.

3.2. Precipitation Water Profiles From Passive Microwave Measurements

[27] The swath of TMI is about 3 times broader than that of the PR, allowing TMI to capture the entire MCS in this case (Figure 1b). Figure 6 shows the overall mean TMI-retrieved precipitation water (PW) profiles of convective and stratiform rain in both the DS and DF sectors. The mean convective rain PW increased toward the surface, while the stratiform rain PW reached its maximum at about the freezing level and then remained almost constant below. Those convective/stratiform characteristics are consistent with the derived PR rain rates, indicating that our convective/stratiform discrimination is reasonable. The mean intensities of PW in the DS sector for both convective and stratiform rain regimes were much weaker than that in the DF sector. The overall suppression of precipitation water in the DS sector is also consistent with the reduction of rain rate detected by PR (Figure 2).

[28] As discussed by *Zipser et al.* [2006], a lower PCT85 is at least statistically related to more intensive updrafts. We used the PCT85 as a proxy of updraft intensity to partially constrain the dynamic impacts on the TMI profiles. As shown in Figure 7, in almost every PCT85 range, the PWs of convective and stratiform rain in the DS sector are significantly smaller than that in the DF sector. This suggests that for a given ice water path aloft at the upper layer, the

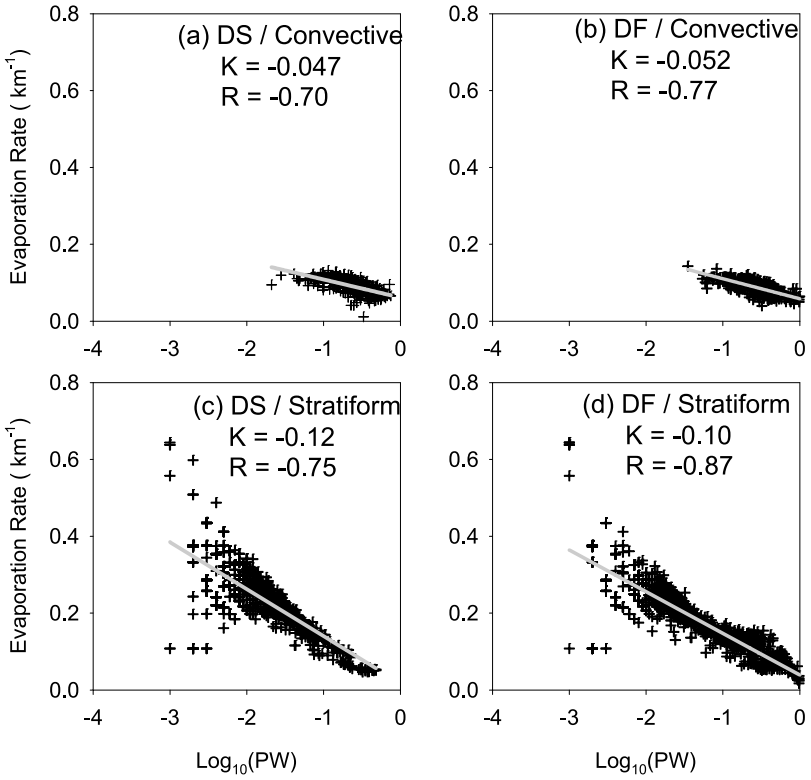

Figure 9. Relationship of evaporation rate against precipitation water (in logarithmic scale) for convective and stratiform rain in (a, c) DS and (b, d) DF sectors for the TMI case study.

precipitation water in the lower layers is generally weaker in the DS sector than in the DF sector. In other words, the ice/water ratio is greater in the DS sector. We speculate that it may be either more small-sized ice particles in the DS sector that are not efficiently converted to precipitation-sized drops, or more precipitation-sized ice particles aloft at the upper layer evaporated during the precipitation.

[29] We also normalized the PW profiles, shown in Figures 8a and 8b, by the near-surface PW, another way to constrain the dynamic variation. Associated PR normalized (at 1.5 km) rain rate (NRR) profiles are also shown in Figures 8c and 8d. Please note that the error bars in Figure 8 are included but are too small to see. For convective rain the normalized PW (NPW) profile in the upper layers is smaller in the DS sector than in the DF sector. The reverse is true for stratiform rains. More apparently, the slope of downward decreasing rate in the stratiform NPW profiles is steeper in the DS sector than in the DF sector, suggesting the roles of mineral dust and/or dry and warm air in the evaporation process below the freezing level. The stratiform NRR profiles show consistent results with TMI NPW.

[30] However, the downward decreasing patterns in convective NPW profiles (Figure 8a) in the DS sector are small and differ substantially from the downward decreasing patterns in the convective NRR profiles (Figure 8c). Since the breakup process (no mass exchange) has a limited effect on TMI PW profiles, different characteristics of observed downward tendency between TMI and PR suggest that a large portion of observed PR rain rate reduction in convective rain in the DS sector may be due to the breakup process rather than to evaporation. The separation of the raindrops' breakup effect from the evaporation effect is very important because the former does not have an impact on the latent heat release while the latter will introduce a cooling effect in ambient air.

[31] To further understand the evaporation process, we defined the evaporation rate (ER) as the slope of a linear regression of the NPW profile between 2 km and the surface. As shown in Figure 9, the ER decreases linearly with the increase of surface precipitation water on a logarithmical scale. The slopes of the evaporation rate against surface

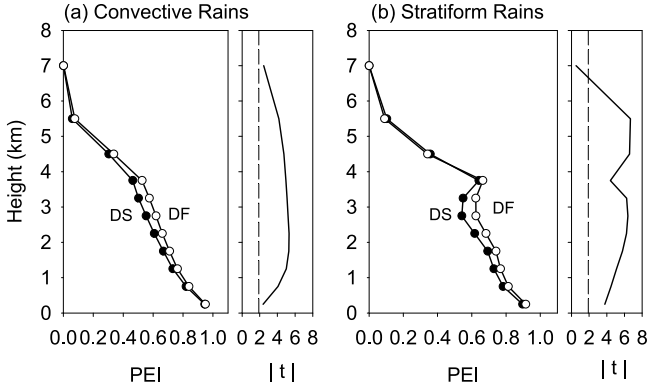

Figure 10. Precipitation efficiency index (PEI) profiles (with standard error) of (a) convective rain and (b) stratiform rain in DS and DF sectors. The *t* testing significances of difference are also shown (dashed line indicates the 95% confidence level at 60 degrees of freedom).

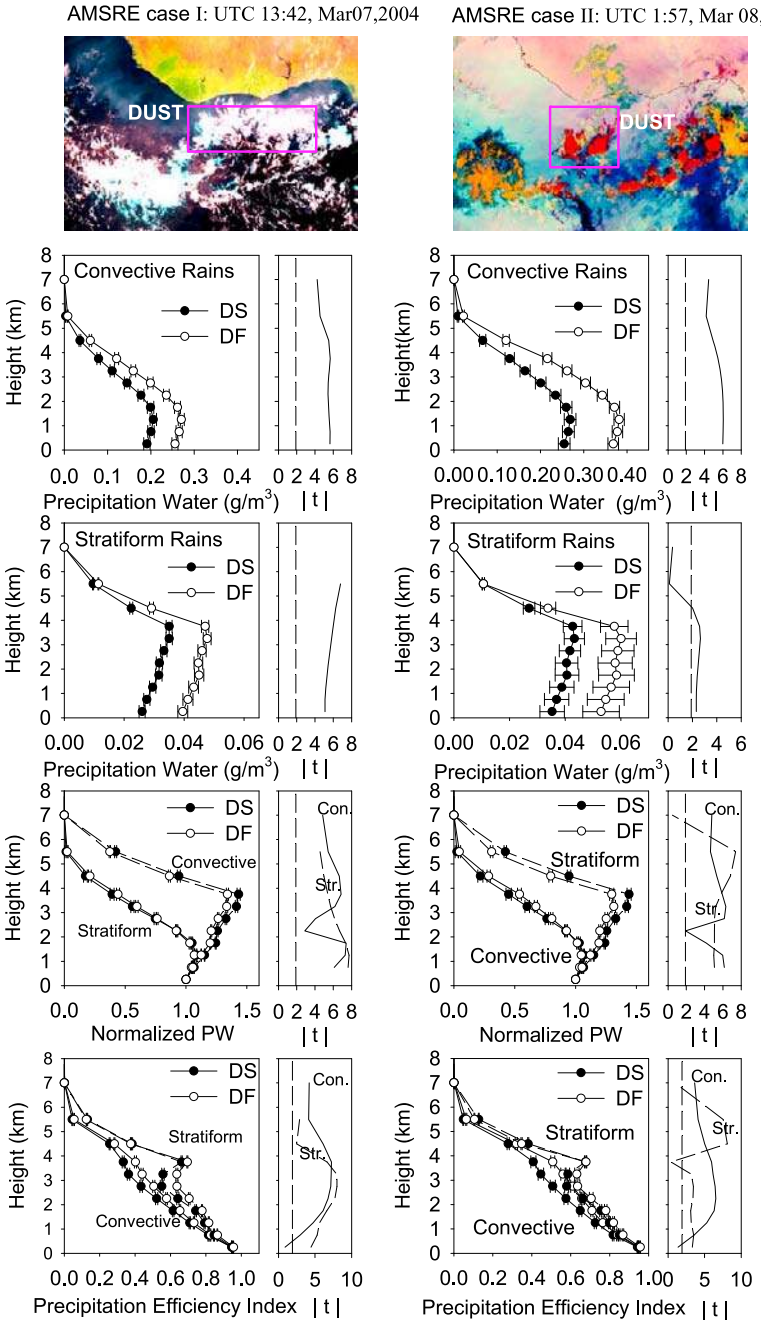

Figure 11. Two other case studies using AMSR-E data. The RGB composite of satellite images taken by Meteosat-8; the mean precipitation water profiles for convective rains; the mean precipitation water profiles for stratiform rains; the normalized precipitation water (PW) profiles for both convective (solid) and stratiform (dashed) rains; and the PEI profiles for both convective (solid) and stratiform (dashed) rain in DS and DF sector in these two cases are given. The *t* testing significances of difference are also shown (dashed line indicates the 95% confidence level at 60 degrees of freedom).

precipitation water are −0.047 (−0.052) for the DS (DF) convective rain and −0.122 (−0.108) for the DS (DF) stratiform rains. It is clear that the slope is greater in the dust-laden sector than in the dust-free sector in the stratiform region, as the drier and warmer dust layer enhances evaporation. However, evaporation rates between the two sectors in the convective regime are not significantly different, most likely because convection and associated turbulence are sufficiently strong to maintain moisture levels in the column. Therefore, we speculate the observed difference of PR rain rates in the convective rain is due mainly to the breakup effect, which may be enhanced by the possible stronger midlevel wind shear [*Dunion and Velden*, 2004] associated with the dust layer. Additionally, from Figure 3, the low-level breakup is more profound for convective rain with larger Hmax30 (i.e., Figures 3b and 3c). As large

Table 2. Slope of Evaporation Rate Against Surface Precipitation Water in Logarithmic Scale Calculated Using TMI and AMSR-E Measurements[a]

		Case Studies			Statistic Studies	
	Sector	TMI	AMSR-E I	AMSR-E II	TMI	AMSR-E
Convective rains	DS	−0.047 (0.70)	−0.051 (0.93)	−0.055 (0.84)	−0.068 (0.74)	−0.054 (0.83)
	DF	−0.052 (0.77)	−0.051 (0.79)	−0.054 (0.80)	−0.065 (0.81)	−0.041 (0.72)
Stratiform rains	DS	−0.122 (0.78)	−0.183 (0.92)	−0.185 (0.92)	−0.170 (0.84)	−0.180 (0.93)
	DF	−0.108 (0.87)	−0.187 (0.95)	−0.169 (0.94)	−0.139 (0.91)	−0.138 (0.93)

[a]Values in parentheses are the correlation efficiency (|R|, all in negative sign) for the linear regression between evaporation rate and surface precipitation water in logarithm scale.

Hamx30 indicate heavy rain rate with large raindrops due to strong updraft intensity, those large raindrops break up easily. Certainly, there are also some hints of evaporation in PR observations. Table 1 lists small percentages of precipitation profiles that have no rain rate at 1.5 km due to raindrops evaporated to water vapor or small droplets out of PR detectable thresholds. The percentage of such pixels is higher in the DS stratiform rain (5.6%) than that in the DF stratiform rain (3.5%). The percentages of such pixels are negligibly small in the convective rains, consistent with TMI measurements.

[32] An important concept of the rain formation process is the precipitation efficiency (PE), which is related to both large-scale convergence of water vapor and the microphysical processes. Efforts have been made to estimate PE by model simulations [*Ferrier et al.*, 1996; *Tao et al.*, 2004]. To explicitly calculate PE requires estimations of the three-dimensional divergence of water vapor for a given cloud system. Thus, it is very difficult to validate the model results. Here we defined an index of precipitation efficiency (PEI) as the ratio of precipitation water to the total of atmospheric hydrometeors:

$$\mathrm{PEI} = \frac{\mathrm{PW}}{\mathrm{CW} + \mathrm{CI} + \mathrm{PW} + \mathrm{PI}}.$$

where CW, CI, PW, and PI stand for cloud water, cloud ice, precipitation water, and precipitation ice, respectively. The PEI provides a measure of conversion efficiency of condensed water vapor to the precipitation water. More importantly, it can be assessed directly from satellite measurements such as TMI retrievals. As shown in Figure 10, the PEI increased toward the Earth at a layer above 4–5 km altitude as more and more ice phase hydrometeors converted to precipitation water. The difference of PEI between the DS and DF sectors was very small at this layer. Below this layer, the PEI was clearly smaller in the DS sector than in the DF sector for both convective and stratiform rain. This suggests that more small cloud particles and precipitating hydrometeors are formed in the cloud system, inhibiting the formation of drizzle and rain and reducing the coalescence efficiency [*Rosenfeld et al.*, 2001]. Also, more precipitation hydrometeors are evaporated and converted to cloud droplets, particularly in the stratiform rain, resulting in an increase of cloud liquid water. Thus, mineral dust tends to decrease the precipitation efficiency for given condensed water in the atmosphere, evidence of the second indirect aerosol effects. This effect may also be influenced by the thermodynamic process of the dry and warm air. The decrease of precipitation efficiency may slow the hydrology cycle process, as more condensed water vapor or cloud water are suspended in the atmosphere for a longer time. It may exert further far-reaching effects on climate.

[33] So far, all the above findings are based on a single case observed by TRMM satellite. To confirm those findings, we also selected two additional cases that were detected by Aqua AMSR-E. As shown in Figure 11 and listed in Table 1, both cases were deep convection systems partially impacted by dust. Although the meteorological conditions and the cloud evolution stage were quite different and the absolute intensity of precipitation water varied from each other, the associated characteristics of precipitation under dust-laden conditions are consistent with the previous TMI analysis, i.e., precipitation at low layers is relatively weaker (Figure 11). The PEI is smaller (Figure 11) and the evaporation is enhanced (Table 2).

3.3. Statistical Analysis

[34] *Petersen and Rutledge* [2001] showed that precipitation in tropical coast areas is relatively stronger than that in isolated oceanic areas. In our case study, the DS sectors were always closer to the African coastal as the dust originated from the Saharan desert. The observed precipitation under the influence of mineral dust, however, was substantially suppressed. Although the regional effect is in favor of our arguments, we would like to further exclude this potential effect by fixing a research domain from 4°N to 1°S and from 10°W to 5°E and by analyzing statistically for the dust-free period (1–4 March) and the dust-laden period (7–10 March). In this fixed area, the numbers of rain profiles detected by TMI and AMSR-E were 7602 and 17,501 during the DS and DF periods, respectively. Also, significant amounts of PR rainfall profiles are analyzed: 1340 in the DS period and 4120 in the DF period, respectively (Table 3). Figure 12 shows the statistical PR rain rate

Table 3. Sample Statistics and Mean Surface Intensity for the Statistic Studies

		Convective Rains		Stratiform Rains		Warm Rains	
	Sector	Sample	Intensity[a]	Sample	Intensity[a]	Sample	Intensity[a]
PR	DS	380	7.93	816	2.09	144	1.12
	DF	1012	14.03	2791	2.91	317	1.47
TMI	DS	838	0.24	1932	0.027		
	DF	958	0.41	2960	0.14		
AMSR-E	DS	1794	0.27	3038	0.064		
	DF	4373	0.43	9210	0.16		

[a]The surface rain intensity stands for mean rain rate (mm/h) for PR but mean precipitation water (g/m^3) for TMI and AMSR-E.

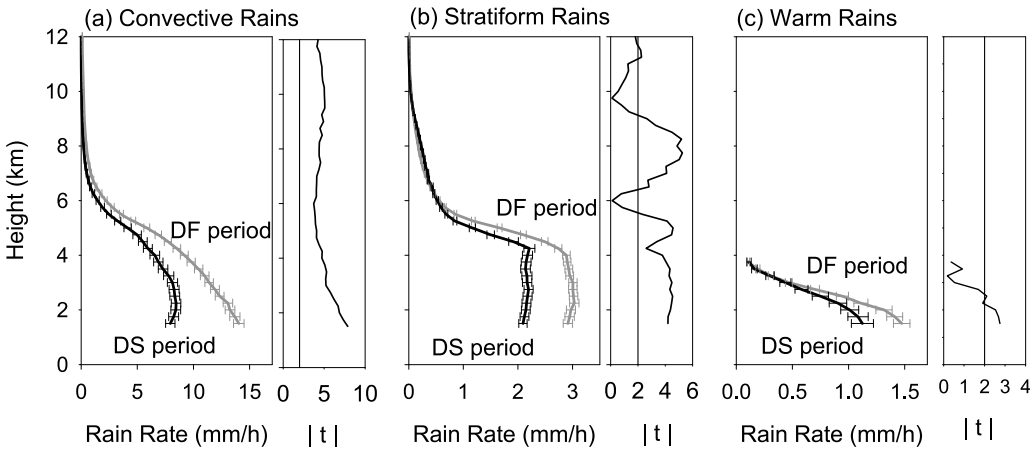

Figure 12. Same as Figure 2 but for the statistical study during DS period (7–10 March 2004) and DF period (1–4 March 2004). The *t* testing significances of difference are also shown (dashed line indicates the 95% confidence level at 60 degrees of freedom).

profiles for convective, stratiform, and warm rain, which are consistent with the profiles of the case study in Figure 2. The stratiform rain rate at high altitudes (above 6 km) was stronger in the DS period than that in the DF period even though the difference is relatively smaller than in the case study. Given the large number of samples in the statistical study, the relatively small difference is still robust and statistically significant. Furthermore, the samples in the statistical study contain different cloud systems at various evolutionary stages and under different meteorological conditions, providing a statistically robust data set for dust-cloud interaction. The enhancement of stratiform rain at high alti-

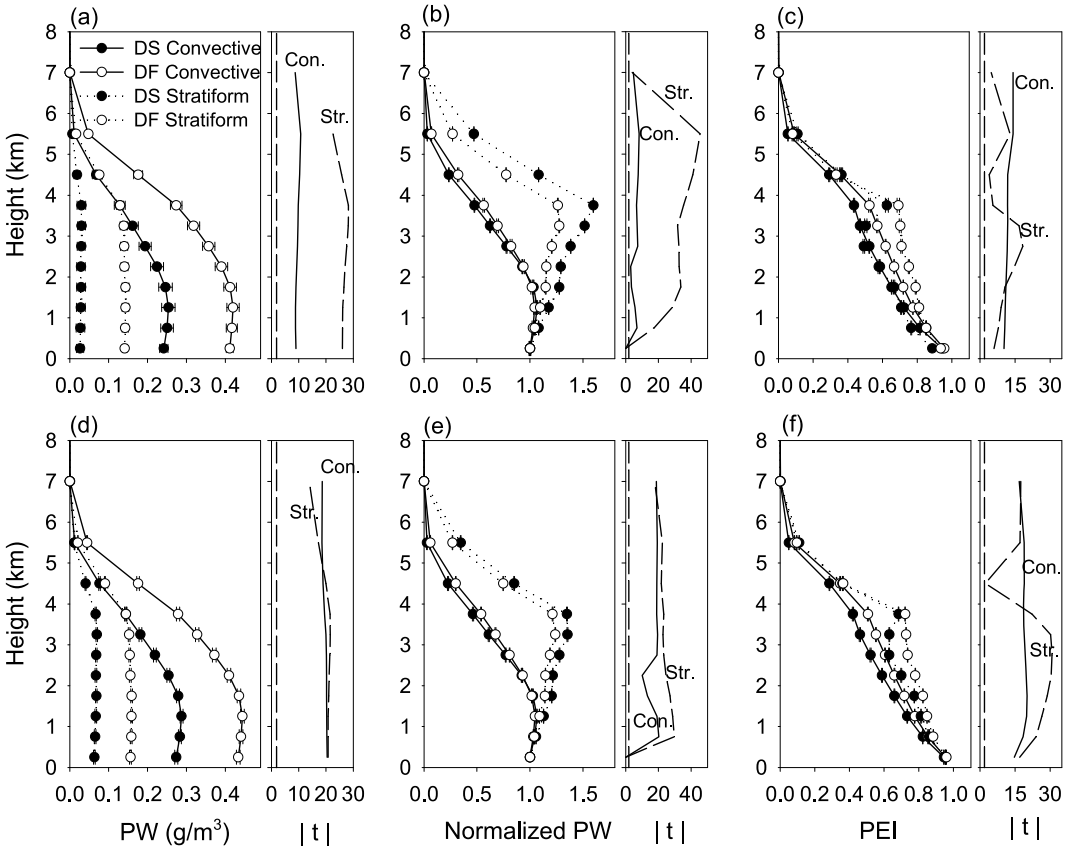

Figure 13. Mean profiles of PW, normalized PW, and precipitation efficiency index during DS period (7–10 March 2004) and DF period (1–4 March 2004) as seen by (a–c) TMI and (d–f) AMSR–E for convective rain and stratiform rains. The *t* testing significances of difference are also shown (dashed line indicates the 95% confidence level at 60 degrees of freedom).

tude is a unique feature of mineral dust impacts on precipitation. Both TMI and AMSR-E statistical PW, NPW, and PEI profiles, shown in Figure 13, clearly corroborate the results of the case study and with each other. We also applied the similar analyses in the statistic study, as we did in the 8 March case study. All results (not show here) are consistent with those from the case study.

4. Discussion and Conclusion

[35] Mineral dust is a significant climate forcing through both direct and indirect effects on climate. Saharan dust and associated dry and warm air substantially influence cloud systems over the Atlantic Ocean from tropical hurricanes to the weather in the southwestern United States. The vertical precipitation profiles reflect the combined effects of dynamic, thermodynamic, and microphysical processes in cloud systems. It is crucial to assess and understand those effects on inner vertical structures of the cloud system. In this paper, we extended the study of *Min et al.* [2009] to more cases by employing observations from both TRMM and Aqua satellites. We also utilized active and passive microwave measurements of precipitation from TRMM PR, TMI, and Aqua AMSR-E to conduct a statistical study. With the uniqueness of passive microwave measurements that combine information of cloud water and precipitation water, we investigated precipitation efficiency and raindrop evaporation process at low altitudes. With the aid of satellite proxy parameters of convective strength, to some extent, we minimized the dynamic and thermodynamic impacts on observed features. The impacts of mineral dust on tropical cloud and precipitation systems are highly dependent on rain type. For convective rain, the patterns of rainfall profiles above the dust layer are determined mainly by updraft intensity. While in the dust layer, for similar updraft intensity, mineral dust and associated warm air enhance the breakup process of raindrops. For stratiform rain, dust-induced microphysical effects are more evident. For similar storm height (or the rain top), precipitation at altitudes above 6 km is enhanced under dust-laden conditions. This may be strong evidence of dust-enhancing ice heterogeneous nucleation. However, precipitation at low altitudes is reduced. For warm rain with similar storm height, precipitation is systematically weaker under dust-laden conditions. We also found that the ratio of precipitation water to the total amount of atmospheric hydrometeors, called precipitation efficiency index, is smaller under dust-laden conditions.

[36] Overall, as indicated by *Min et al.* [2009], more small-sized cloud particles and precipitating hydrometeors are formed in the dust-laden cloud system. This can be explained if mineral dust acts as additional cloud condensation nuclei and ice nuclei, which can enhance precipitation at high altitude, inhibit drizzle formation, and result in small precipitation efficiency index. The decrease of precipitation efficiency indicates more condensed water vapor or cloud water suspended in the atmosphere. Thus, mineral dust exhibits a possible second aerosol indirect effect on cloud and precipitation systems. The evaporation rate increases with decreasing surface precipitation water. The dust-induced microphysical effects are also clear in warm rain, and dust particles suppress rain rate at all heights and may decrease warm rain occurrence.

[37] Completely separating microphysical effects from dynamic effects in an observational study of aerosol indirect effects is difficult, particularly using only remotely sensed measurements. We attempted to minimize the dynamic and thermodynamic induced effects by several steps, including comparing rainfall features in different portions of one single MCS rather than different systems, separating samples into convective and stratiform rain regimes, and segregating measurements using proxy parameters of updraft intensity. Even so, our conclusion, like many others, may not completely exclude the dynamic and thermodynamic influences. Furthermore, uncertainties from the active and passive microwave retrievals of rainfall vertical structure warrant further study. For active microwave radar, the biggest issue is potential changes in drop size distribution of rainfall due to the presence of mineral dust. It affects both the attenuation correction procedure and the Ze-R conversion procedure. For passive microwave radiometer, the accuracy of retrieved hydrometeor profiles strongly depends on the preexisting profile database and the inverse procedure.

[38] Nonetheless, the consistency of our results from analyses of multisensor observation in both case and statistical studies gives us confidence that the observed changes of precipitation vertical structure are likely due to mineral dust indirect effects. If confirmed, strong mineral dust indirect effects will have far-reaching impacts on climate, as global warming and anthropogenic activity will substantially alter loading and distribution of atmospheric mineral dust [*Tegen et al.*, 2004; *Yoshioka et al.*, 2005].

[39] **Acknowledgments.** The authors thank C. Kummerow and J. Crook for the precipitation profile data of AMSR-E, EUMETSAT for Meteosat-8 data and associated image processing tools, and NASA for TRMM Orbit Viewer. Constructive suggestions and comments from three anonymous reviewers are acknowledged. This research was supported by the Office of Science (BER), U.S. Department of Energy, through the Atmospheric Radiation Measurement (ARM) grant DE-FG02-03ER63531 and by the NOAA Educational Partnership Program with Minority Serving Institutions (EPP/MSI) under cooperative agreements NA17AE1625 and NA17AE1623. R.L. was also supported by National Natural Science Foundation of China (NSFC) grants 40605010.

References

Andreae, M. O., D. Rosenfeld, P. Artaxo, A. A. Costa, G. P. Frank, K. M. Longo, and M. A. F. Silva-Dias (2004), Smoke rain clouds over the Amazon, *Science*, *303*, 1337–1342, doi:10.1126/science.1092779.

Awaka, J., T. Iguchi, H. Kumagai, and K. Okamoto (1997), Rain type classification algorithm for TRMM precipitation radar, paper presented at IEEE 1997 International Geoscience Remote Sensing Symposium, Singapore, 3–8 Aug.

Cecil, D. J., S. J. Goodman, D. J. Boccippio, E. J. Zipser, and S. W. Nesbitt (2005), Three years of TRMM precipitation features. Part I: Radar, radiometric, and lightning characteristics, *Mon. Weather Rev.*, *133*, 543–566, doi:10.1175/MWR-2876.1.

DeMott, P. J., K. Sassen, M. R. Poellot, D. Baumgardner, D. C. Rogers, S. D. Brooks, A. J. Prenni, and S. M. Kreidenweis (2003), African dust aerosols as atmospheric ice nuclei, *Geophys. Res. Lett.*, *30*(14), 1732, doi:10.1029/2003GL017410.

Denman, K. L., et al. (2007), Couplings between changes in the climate system and biogeochemistry, in *Climate Change 2007: The Physical Science Basis. Contribution of Working Group I to the Fourth Assessment Report of the Intergovernmental Panel on Climate Change*, edited by S. Solomon et al., pp. 488–587, Cambridge Univ. Press, Cambridge, U. K.

Dunion, J. P., and C. S. Velden (2004), The impact of the Saharan air layer on Atlantic tropical cyclone activity, *Bull. Am. Meteorol. Soc.*, *85*, 353–365, doi:10.1175/BAMS-85-3-353.

Ferrier, B. S., J. Simpson, and W.-K. Tao (1996), Factors responsible for precipitation efficiencies in mid-latitude and tropical squall simulations, *Mon. Weather Rev.*, *124*, 2100–2125, doi:10.1175/1520-0493(1996)124<2100:FRFPEI>2.0.CO;2.

Forster, P., et al. (2007), Changes in atmospheric constituents and in radiative forcing, in *Climate Change 2007: The Physical Science Basis. Contribution of Working Group I to the Fourth Assessment Report of the Intergovernmental Panel on ClimateChange*, edited by S. Solomon et al., pp. 129–234, Cambridge Univ. Press, Cambridge, U. K.

Fu, Y., and G. Liu (2001), The variability of tropical precipitation profiles and its impact on microwave brightness temperatures as inferred from TRMM Data, *J. Appl. Meteorol.*, *40*(12), 2130–2143, doi:10.1175/1520-0450(2001)040<2130:TVOTPP>2.0.CO;2.

Generoso, S., I. Bey, M. Labonne, and F.-M. Bre'on (2008), Aerosol vertical distribution in dust outflow over the Atlantic: Comparisons between GEOS-Chem and Cloud-Aerosol Lidar and Infrared Pathfinder Satellite Observation (CALIPSO), *J. Geophys. Res.*, *113*, D24209, doi:10.1029/2008JD010154.

Ginoux, P., J. M. Prospero, O. Torres, and M. Chin (2004), Long-term simulation of global dust distribution with the GOCART model: Correlation with North Atlantic Oscillation, *Environ. Model. Softw.*, *19*(2), 113–128, doi:10.1016/S1364-8152(03)00114-2.

Haynes, P. H., and M. E. McIntyre (1987), On the evolution of vorticity and potential vorticity in the presence of diabatic heating and frictional or other forces, *J. Atmos. Sci.*, *44*, 828–841, doi:10.1175/1520-0469(1987)044<0828:OTEOVA>2.0.CO;2.

Haywood, J., and O. Boucher (2000), Estimates of the direct and indirect radiative forcing due to tropospheric aerosols: A review, *Rev. Geophys.*, *38*(4), 513–543, doi:10.1029/1999RG000078.

Houze, R. A. (1997), Stratiform precipitation in regions of convection: A meteorological paradox?, *Bull. Am. Meteorol. Soc.*, *78*, 2179–2196, doi:10.1175/1520-0477(1997)078<2179:SPIROC>2.0.CO;2.

Iguchi, T., T. Kozu, R. Meneghini, J. Awaka, and K. Okamoto (2000), Rain-profiling algorithm for the TRMM precipitation radar, *J. Appl. Meteorol.*, *39*(12), 2038–2052, doi:10.1175/1520-0450(2001)040<2038:RPAFTT>2.0.CO;2.

Kummerow, C., W. Barnes, T. Kozu, J. Shiue, and J. Simpson (1998), The Tropical Rainfall Measuring Mission (TRMM) sensor package, *J. Atmos. Oceanic Technol.*, *15*, 809817, doi:10.1175/1520-0426(1998)015<0809:TTRMMT>2.0.CO;2.

Kummerow, C., et al. (2000), The status of the Tropical Rainfall Measuring Mission (TRMM) after two years in orbit, *J. Appl. Meteorol.*, *39*(12), 1965–1982, doi:10.1175/1520-0450(2001)040<1965:TSOTTR>2.0.CO;2.

Kummerow, C., et al. (2001), The evolution of the Goddard profiling algorithm (GPROF) for rainfall estimation from passive microwave sensors, *J. Appl. Meteorol.*, *40*(11), 1801–1820, doi:10.1175/1520-0450(2001)040<1801:TEOTGP>2.0.CO;2.

Liu, G., and Y. Fu (2001), The characteristics of tropical precipitation profiles as inferred from satellite radar measurements, *J. Meteorol. Soc. Jpn.*, *79*(1), 131–143, doi:10.2151/jmsj.79.131.

Liu, D., Z. Wang, Z. Liu, D. Winker, and C. Trepte (2008), A height resolved global view of dust aerosols from the first year CALIPSO lidar measurements, *J. Geophys. Res.*, *113*, D16214, doi:10.1029/2007JD009776.

Liu, Z., et al. (2008), CALIPSO lidar observations of the optical properties of Saharan dust: A case study of long-range transport, *J. Geophys. Res.*, *113*, D07207, doi:10.1029/2007JD008878.

Mapes, B. E., and R. A. Houze (1995), Diabatic divergence profiles in western Pacific mesoscale convective systems, *J. Atmos. Sci.*, *52*, 1807–1828, doi:10.1175/1520-0469(1995)052<1807:DDPIWP>2.0.CO;2.

Min, Q.-L., R. Li, B. Lin, E. Joseph, S. Wang, Y. Hu, V. Morris, and F. Chang (2009), Evidence of mineral dust altering cloud microphysics and precipitation, *Atmos. Chem. Phys.*, *9*, 3223–3231.

Morris, V., P. Clemente-Colón, N. R. Nalli, E. Joseph, R. A. Armstrong, Y. Detrés, M. D. Goldberg, P. J. Minnett, and R. Lumpkin (2006), Measuring Trans-Atlantic aerosol transport from Africa, *Eos Trans. AGU*, *87*(50), doi:10.1029/2006EO500001.

Nalli, N. R., et al. (2005), Profile observations of the Saharan air layer during AEROSE 2004, *Geophys. Res. Lett.*, *32*, L05815, doi:10.1029/2004GL022028.

Nalli, N. R., et al. (2006), Ship-based measurements for infrared sensor validation during Aerosol and Ocean Science Expedition 2004, *J. Geophys. Res.*, *111*, D09S04, doi:10.1029/2005JD006385.

Nesbitt, S. W., and D. J. Cecil (2000), A census of precipitation features in the Tropics using TRMM: Radar, ice scattering, and ice observations, *J. Clim.*, *13*, 4087–4106, doi:10.1175/1520-0442(2000)013<4087:ACOPFI>2.0.CO;2.

Petersen, W. A., and S. A. Rutledge (2001), Regional variability in tropical convection: Observations from TRMM, *J. Clim.*, *14*(17), 3566–3586, doi:10.1175/1520-0442(2001)014<3566:RVITCO>2.0.CO;2.

Prospero, J. M. (1999), Long-term measurements of the transport of African mineral dust to the southeastern United States: Implications for regional air quality, *J. Geophys. Res.*, *104*(D13), 15,917–15,928, doi:10.1029/1999JD900072.

Rosenfeld, D. (1999), TRMM observed first direct evidence of smoke from forest fires inhibiting rainfall, *Geophys. Res. Lett.*, *26*(20), 3105–3108, doi:10.1029/1999GL006066.

Rosenfeld, D. (2000), Suppression of rain and snow by urban and industrial air pollution, *Science*, *287*, 1793–1796, doi:10.1126/science.287.5459.1793.

Rosenfeld, D., Y. Rudich, and R. Lahav (2001), Desert dust suppressing precipitation: A possible desertification feedback loop, *Proc. Natl. Acad. Sci. U. S. A.*, *98*(11), 5975–5980, doi:10.1073/pnas.101122798.

Rosenfeld, D., U. Lohmann, G. B. Raga, C. D. O'Dowd, M. Kulmala, S. Fuzzi, A. Reissell, and M. O. Andreae (2008), Flood or drought: How do aerosols affect precipitation?, *Science*, *321*, 1309–1313, doi:10.1126/science.1160606.

Sassen, K. (2005), Meteorology: Dusty ice clouds over Alaska, *Nature*, *434*(7032), 456, doi:10.1038/434456a.

Sassen, K., P. J. DeMott, J. M. Prospero, and M. R. Poellot (2003), Saharan dust storms and indirect aerosol effects on clouds: CRYSTAL-FACE results, *Geophys. Res. Lett.*, *30*(12), 1633, doi:10.1029/2003GL017371.

Steiner, M., R. A. Houze Jr., and S. Yuter (1995), Climatological characterization of three-dimensional storm structure from operational radar and rain gauge data, *J. Appl. Meteorol.*, *34*, 1978–2007, doi:10.1175/1520-0450(1995)034<1978:CCOTDS>2.0.CO;2.

Tao, W. K., D. Johnson, C. L. Shie, and J. Simpson (2004), The atmospheric energy budget and large-scale precipitation efficiency of convective systems during TOGA COARE, GATE, SCSMEX, and ARM: Cloud-resolving model simulations, *J. Atmos. Sci.*, *61*, 2405–2423, doi:10.1175/1520-0469(2004)061<2405:TAEBAL>2.0.CO;2.

Tegen, I., M. Werner, S. P. Harrison, and K. E. Kohfeld (2004), Relative importance of climate and land use in determining present and future global soil dust emission, *Geophys. Res. Lett.*, *31*, L05105, doi:10.1029/2003GL019216.

Teller, A., and Z. Levin (2006), The effects of aerosols on precipitation and dimensions of subtropical clouds: A sensitivity study using a numerical cloud model, *Atmos. Chem. Phys.*, *6*, 67–80.

Twomey, S. (1977), The influence of pollution on the shortwave albedo of clouds, *J. Atmos. Sci.*, *34*, 1149–1152.

Ulbrich, C. W., and D. Atlas (2007), Microphysics of raindrop size spectra: Tropical continental and maritime storms, *J. Appl. Meteorol. Climatol.*, *46*, 1777–1791.

Ulbrich, C. W., and D. Atlas (2008), Radar measurement of rainfall with and without polarimetry, *J. Appl. Meteorol. Climatol.*, *47*, 1929–1939, doi:10.1175/2007JAMC1804.1.

van den Heever, S. C., G. G. Carrió, W. R. Cotton, P. J. DeMott, and A. J. Prenni (2006), Impacts of nucleating aerosol on Florida storms. Part I: Mesoscale Simulations, *J. Atmos. Sci.*, *63*, 1752–1775, doi:10.1175/JAS3713.1.

Wu, Z., and E. S. Sarachik (2000), Vertical structure of convective heating and the three-dimensional structure of the forced circulation on an equatorial beta plane, *J. Atmos. Sci.*, *57*, 2169–2187, doi:10.1175/1520-0469(2000)057<2169:VSOCHA>2.0.CO;2.

Yin, Y., Z. Levin, T. G. Reisin, and S. Tzivion (2000), The effect of giant cloud condensation nuclei on the development of precipitation in convective clouds–A numerical study, *Atmos. Res.*, *53*, 91–116, doi:10.1016/S0169-8095(99)00046-0.

Yoshioka, M., N. Mahowald, J. L. Dufresne, and C. Luo (2005), Simulation of absorbing aerosol indices for African dust, *J. Geophys. Res.*, *110*, D18S17, doi:10.1029/2004JD005276.

Zipser, E. J., D. J. Cecil, C. Liu, S. W. Nesbitt, and D. P. Yorty (2006), Where are the most intensive thunderstorm on Earth?, *Bull. Am. Meteorol. Soc.*, *87*, 1057–1071, doi:10.1175/BAMS-87-8-1057.

R. Li and Q.-L. Min, Atmospheric Sciences Research Center of the State University of New York at Albany, 251 Fuller Rd., Albany, NY 12201 USA. (min@asrc.cestm.albany.edu)